

RESEARCH ARTICLE | JUNE 07 2023

Attojoule/bit folded thin film lithium niobate coherent modulators using air-bridge structures

Mengyue Xu ; Yuntao Zhu ; Jin Tang; Jingyi Wang; Lin Liu; Huixiao Ma ; Siyuan Yu; Bofang Zheng ; Xinlun Cai



APL Photonics 8, 066104 (2023)

<https://doi.org/10.1063/5.0146987>



View
Online



Export
Citation

CrossMark

AMERICAN ELEMENTS

THE ADVANCED MATERIALS MANUFACTURER

sapphire windows	Nd:YAG	yttrium iron garnet	glassy carbon	beamsplitters	fused quartz	additive manufacturing
spintronics	raman substrates	zeolites	III-IV semiconductors	gallium lump	copper nanoparticles	organometallics
silver nanoparticles	perovskites	nano ribbons	barium fluoride	europlum phosphors	photronics	infrared dyes
MOICVD	beta-barium borate	epitaxial crystal growth	ultra high purity materials	He	transparent ceramics	CIGS
rare earth metals	quantum dots	cerium oxide polishing powder		B	cermet	nanodispersions
osmium	scintillation Ce:YAG	surface functionalized nanoparticles		C	MBE grade materials	thin film
refractory metals	laser crystals	Al	Ge	N	OLED lighting	solar energy
anodized aluminum niobate	InAs wafers	Si	As	P	Europium phosphors	g-polarizers
perovskite crystals	MOFs	Sn	Sb	S	transparent ceramics	fiber optics
	AuNPs	Tb	Yb	Cl	ceramic	h-BN
	ZnS	Hf	Tm	Kr	nanodispersions	deposition slugs
	CdTe	Tz	Dy	I	MBE grade materials	photovoltaics
		V	Ho	Xe	transparent ceramics	CVD precursors
		Cr	Eu		cermet	h-BN
		Mn	Gd		nanodispersions	deposition slugs
		Fe	Tb		MBE grade materials	photovoltaics
		Co	Dy		transparent ceramics	CVD precursors
		Ni	Ho		ceramic	h-BN
		Cu	Eu		nanodispersions	deposition slugs
		Zn	Tm		MBE grade materials	photovoltaics
		Al	Yb		transparent ceramics	CVD precursors
		Si			cermet	h-BN
		Sn			nanodispersions	deposition slugs
		Tb			MBE grade materials	photovoltaics
		Hf			transparent ceramics	CVD precursors
		Tz			ceramic	h-BN
		V			nanodispersions	deposition slugs
		Cr			MBE grade materials	photovoltaics
		Mn			transparent ceramics	CVD precursors
		Fe			cermet	h-BN
		Co			nanodispersions	deposition slugs
		Ni			MBE grade materials	photovoltaics
		Cu			transparent ceramics	CVD precursors
		Zn			ceramic	h-BN
		Al			nanodispersions	deposition slugs
		Si			MBE grade materials	photovoltaics
		Sn			transparent ceramics	CVD precursors
		Tb			cermet	h-BN
		Hf			nanodispersions	deposition slugs
		Tz			MBE grade materials	photovoltaics
		V			transparent ceramics	CVD precursors
		Cr			ceramic	h-BN
		Mn			nanodispersions	deposition slugs
		Fe			MBE grade materials	photovoltaics
		Co			transparent ceramics	CVD precursors
		Ni			cermet	h-BN
		Cu			nanodispersions	deposition slugs
		Zn			MBE grade materials	photovoltaics
		Al			transparent ceramics	CVD precursors
		Si			ceramic	h-BN
		Sn			nanodispersions	deposition slugs
		Tb			MBE grade materials	photovoltaics
		Hf			transparent ceramics	CVD precursors
		Tz			cermet	h-BN
		V			nanodispersions	deposition slugs
		Cr			MBE grade materials	photovoltaics
		Mn			transparent ceramics	CVD precursors
		Fe			ceramic	h-BN
		Co			nanodispersions	deposition slugs
		Ni			MBE grade materials	photovoltaics
		Cu			transparent ceramics	CVD precursors
		Zn			cermet	h-BN
		Al			nanodispersions	deposition slugs
		Si			MBE grade materials	photovoltaics
		Sn			transparent ceramics	CVD precursors
		Tb			ceramic	h-BN
		Hf			nanodispersions	deposition slugs
		Tz			MBE grade materials	photovoltaics
		V			transparent ceramics	CVD precursors
		Cr			cermet	h-BN
		Mn			nanodispersions	deposition slugs
		Fe			MBE grade materials	photovoltaics
		Co			transparent ceramics	CVD precursors
		Ni			ceramic	h-BN
		Cu			nanodispersions	deposition slugs
		Zn			MBE grade materials	photovoltaics
		Al			transparent ceramics	CVD precursors
		Si			cermet	h-BN
		Sn			nanodispersions	deposition slugs
		Tb			MBE grade materials	photovoltaics
		Hf			transparent ceramics	CVD precursors
		Tz			cermet	h-BN
		V			nanodispersions	deposition slugs
		Cr			MBE grade materials	photovoltaics
		Mn			transparent ceramics	CVD precursors
		Fe			ceramic	h-BN
		Co			nanodispersions	deposition slugs
		Ni			MBE grade materials	photovoltaics
		Cu			transparent ceramics	CVD precursors
		Zn			cermet	h-BN
		Al			nanodispersions	deposition slugs
		Si			MBE grade materials	photovoltaics
		Sn			transparent ceramics	CVD precursors
		Tb			cermet	h-BN
		Hf			nanodispersions	deposition slugs
		Tz			MBE grade materials	photovoltaics
		V			transparent ceramics	CVD precursors
		Cr			ceramic	h-BN
		Mn			nanodispersions	deposition slugs
		Fe			MBE grade materials	photovoltaics
		Co			transparent ceramics	CVD precursors
		Ni			ceramic	h-BN
		Cu			nanodispersions	deposition slugs
		Zn			MBE grade materials	photovoltaics
		Al			transparent ceramics	CVD precursors
		Si			cermet	h-BN
		Sn			nanodispersions	deposition slugs
		Tb			MBE grade materials	photovoltaics
		Hf			transparent ceramics	CVD precursors
		Tz			cermet	h-BN
		V			nanodispersions	deposition slugs
		Cr			MBE grade materials	photovoltaics
		Mn			transparent ceramics	CVD precursors
		Fe			ceramic	h-BN
		Co			nanodispersions	deposition slugs
		Ni			MBE grade materials	photovoltaics
		Cu			transparent ceramics	CVD precursors
		Zn			cermet	h-BN
		Al			nanodispersions	deposition slugs
		Si			MBE grade materials	photovoltaics
		Sn			transparent ceramics	CVD precursors
		Tb			cermet	h-BN
		Hf			nanodispersions	deposition slugs
		Tz			MBE grade materials	photovoltaics
		V			transparent ceramics	CVD precursors
		Cr			ceramic	h-BN
		Mn			nanodispersions	deposition slugs
		Fe			MBE grade materials	photovoltaics
		Co			transparent ceramics	CVD precursors
		Ni			ceramic	h-BN
		Cu			nanodispersions	deposition slugs
		Zn			MBE grade materials	photovoltaics
		Al			transparent ceramics	CVD precursors
		Si			cermet	h-BN
		Sn			nanodispersions	deposition slugs
		Tb			MBE grade materials	photovoltaics
		Hf			transparent ceramics	CVD precursors
		Tz			cermet	h-BN
		V			nanodispersions	deposition slugs
		Cr			MBE grade materials	photovoltaics
		Mn			transparent ceramics	CVD precursors
		Fe			ceramic	h-BN
		Co			nanodispersions	deposition slugs
		Ni			MBE grade materials	photovoltaics
		Cu			transparent ceramics	CVD precursors
		Zn			cermet	h-BN
		Al			nanodispersions	deposition slugs
		Si			MBE grade materials	photovoltaics
		Sn			transparent ceramics	CVD precursors
		Tb			cermet	h-BN
		Hf			nanodispersions	deposition slugs
		Tz			MBE grade materials	photovoltaics
		V			transparent ceramics	CVD precursors
		Cr			ceramic	h-BN
		Mn			nanodispersions	deposition slugs
		Fe			MBE grade materials	photovoltaics
		Co			transparent ceramics	CVD precursors
		Ni			ceramic	h-BN
		Cu			nanodispersions	deposition slugs
		Zn			MBE grade materials	photovoltaics
		Al			transparent ceramics	CVD precursors
		Si			cermet	h-BN
		Sn			nanodispersions	deposition slugs
		Tb			MBE grade materials	photovoltaics
		Hf			transparent ceramics	CVD precursors
		Tz			cermet	h-BN
		V			nanodispersions	deposition slugs
		Cr			MBE grade materials	photovoltaics
		Mn			transparent ceramics	CVD precursors
		Fe			ceramic	h-BN
		Co			nanodispersions	deposition slugs
		Ni			MBE grade materials	photovoltaics
		Cu			transparent ceramics	CVD precursors
		Zn			cermet	h-BN
		Al			nanodispersions	deposition slugs
		Si			MBE grade materials	photovoltaics
		Sn			transparent ceramics	CVD precursors
		Tb			cermet	h-BN
		Hf			nanodispersions	deposition slugs
		Tz			MBE grade materials	photovoltaics
		V			transparent ceramics	CVD precursors
		Cr			ceramic	h-BN
		Mn			nanodispersions	deposition slugs
		Fe			MBE grade materials	photovoltaics
		Co			transparent ceramics	CVD precursors
		Ni			ceramic	h-BN
		Cu			nanodispersions	deposition slugs
		Zn			MBE grade materials	photovoltaics
		Al			transparent ceramics	CVD precursors
		Si			cermet	h-BN
		Sn			nanodispersions	deposition slugs
		Tb			MBE grade materials	photovoltaics
		Hf			transparent ceramics	CVD precursors
		Tz			cermet	h-BN
		V			nanodispersions	deposition slugs
		Cr			MBE grade materials	photovoltaics
		Mn			transparent ceramics	CVD precursors
		Fe			ceramic	h-BN
		Co			nanodispersions	deposition slugs
		Ni			MBE grade materials	photovoltaics
		Cu			transparent ceramics	CVD precursors
		Zn			cermet	h-BN
		Al			nanodispersions	deposition slugs
		Si			MBE grade materials	photovoltaics
		Sn			transparent ceramics	CVD precursors
		Tb			cermet	h-BN
		Hf			nanodispersions	deposition slugs
		Tz			MBE grade materials	photovoltaics
		V			transparent ceramics	CVD precursors
		Cr			ceramic	h-BN
		Mn			nanodispersions	deposition slugs
		Fe			MBE grade materials	photovoltaics
		Co			transparent ceramics	CVD precursors
		Ni			ceramic	h-BN
		Cu			nanodispersions	deposition slugs
		Zn			MBE grade materials	photovoltaics
		Al			transparent ceramics	CVD precursors
		Si			cermet	h-BN
		Sn			nanodispersions	deposition slugs
		Tb			MBE grade materials	photovoltaics
		Hf			transparent ceramics	CVD precursors
		Tz			cermet	h-BN
		V			nanodispersions	deposition slugs
		Cr			MBE grade materials	photovoltaics
		Mn			transparent ceramics	CVD precursors
		Fe			ceramic	h-BN
		Co			nanodispersions	deposition slugs
		Ni			MBE grade materials	photovoltaics
		Cu			transparent ceramics	CVD precursors
		Zn			cermet	h-BN
		Al			nanodispersions	deposition slugs
		Si			MBE grade materials	photovoltaics
		Sn			transparent ceramics	CVD precursors
		Tb			cermet	h-BN
		Hf			nanodispersions	deposition slugs
		Tz			MBE grade materials	photovoltaics
		V			transparent ceramics	C

Attojoule/bit folded thin film lithium niobate coherent modulators using air-bridge structures

Cite as: APL Photon. 8, 066104 (2023); doi: 10.1063/5.0146987

Submitted: 17 February 2023 • Accepted: 24 May 2023 •

Published Online: 7 June 2023



View Online



Export Citation



CrossMark

Mengyue Xu,¹ Yuntao Zhu,¹ Jin Tang,² Jingyi Wang,¹ Lin Liu,¹ Huixiao Ma,² Siyuan Yu,¹ Bofang Zheng,² and Xinlun Cai^{1,3,a}

AFFILIATIONS

¹ State Key Laboratory of Optoelectronic Materials and Technologies and School of Electronics and Information Technology, Sun Yat-sen University, Guangzhou 510275, China

² 2012 Labs, Huawei Technologies Co., Ltd., Shenzhen 518129, China

³ Hefei National Laboratory, Hefei 230088, China

^a Author to whom correspondence should be addressed: caixlun5@mail.sysu.edu.cn

ABSTRACT

Coherent technology has been employed in long-haul transmission systems in the past decade, with growing demand for capacity at ever-lower costs per bit. High-performance coherent modulators with high data rates, wide bandwidth, small footprint, and low power operation are highly desired. Toward this end, we propose a folded thin-film lithium niobate (TFLN) dual-polarization in-phase quadrature modulator featuring a low half-wave voltage of 1 V and a compact footprint of $4 \times 8 \text{ mm}^2$. To suppress RF wavefront distortion and optimize high-frequency electro-optic performance, we utilize air-bridge structures in the U-turns of the traveling-wave electrodes. As a demonstration of the long-haul transmission capacities with our device, we present driverless 703 Gb/s/ λ line-rate transmissions, with a subcarrier modulation scheme, over a 1120 km single-mode fiber link. Here, for the first time, to our knowledge, our device allows for attojoule-per-bit level electrical energy consumption over transmission distances above 1000 km. The device opens opportunities for much lower-cost and capacity-intensive coherent systems that consume ultra-low power, support high data rate, and work in small spaces.

© 2023 Author(s). All article content, except where otherwise noted, is licensed under a Creative Commons Attribution (CC BY) license (<http://creativecommons.org/licenses/by/4.0/>). <https://doi.org/10.1063/5.0146987>

16 November 2023 03:26:04

I. INTRODUCTION

With the rapid development of coherent technology, one of the primary tasks is to maximize reach–capacity product and minimize power consumption with the least parallel electro-optic (EO) interfaces, which means that we need to push coherent transceivers to higher capacity and lower cost per bit.^{1,2} The bottleneck to achieving these is to find EO modulators that have higher bit rates per wavelength, lower power consumption, smaller device size, and longer optical reach in coherent transceivers. Several material platforms have shown distinct advantages as strong candidates for next-generation coherent modulators in long-haul links, such as silicon photonics,^{3,4} indium phosphine,^{5,6} gallium arsenide,⁷ and lithium niobate (LN).⁸ Among them, LN can offer a linear Pockels effect, a wide transparency window, and less wavelength independence,

which makes LN modulators extra competitive in long-haul networks. However, the bulkiness of the device, large power consumption, and limited transmission capacity of conventional LN result in unsatisfactory performance and high operating expenditures.

Recently, thin-film lithium niobate (TFLN) modulators exhibit considerable promise in achieving low drive voltages, ultra-high bandwidths, and smaller footprints.^{9–17} However, to achieve a driving voltage of less than 1 V, a fairly long modulation section ($>20 \text{ mm}$) would be required owing to the moderate EO coefficient of the TFLN material.⁹ Such lengths pose challenges for compact coherent transceiver modules and difficulties in developing high-density photonic integrated circuits. Recently, folded structures have been demonstrated in TFLN modulators to reduce the geometric length of the device while maintaining a low driving voltage.^{13–17} To date, the existing folded modulators exhibit a compromised

frequency response, with limited bandwidths of <50 GHz and a relatively large RF return loss of -10 dB, which can be attributed to the distortion of the RF wavefront in the U-turns of the folded traveling wave electrodes (TWEs).^{18–22} Most recently, a ring-assisted modulator has demonstrated a significantly improved modulation efficiency (0.35 V·cm) and broad bandwidth in a compact size.¹⁰ However, the working principle of the device requires that the wavelength of the input lightwave must align carefully to achieve the right coupling condition of the ring, making it cumbersome to use and less friendly for coherent wavelength-division multiplexing (WDM) applications.

Herein, we propose folded dual-polarization in-phase quadrature (DP-IQ) TFLN modulators featuring a low half-wave voltage of 1 V and a compact footprint of 4×8 mm². The devices contain four folded Mach-Zehnder modulators (MZMs) with meandered capacitance-loaded traveling-wave electrodes (CL-TWEs). Importantly, we utilize air-bridge structures in the U-turns of the TWEs, which greatly suppresses RF wavefront distortion, leading to a large bandwidth of >67 GHz and a low RF return loss of <-15 dB. We evaluate our device in a coherent WDM system with the other ten channels in the Nyquist subcarrier scheme. Owing to the low half-wave voltage (V_{π}) and large bandwidth, the device supports driverless 703 Gb/s line-rate transmissions over a 1120 km single-mode fiber link with 479 aJ/bit electrical power consumption. This is the first demonstration of a long-haul transmission over 1000 km optical links with aJ/bit energy efficiency.

II. DEVICE STRUCTURE, DESIGN, AND FABRICATION

As shown in Fig. 1(a), we integrated four folded MZMs with a low-loss and low-crosstalk on-chip polarization rotator and combiner (PRC)⁹ to build up a DP-IQ. Four folded MZMs with meandered CL-TWEs shared adjacent ground electrodes, of which each consists of three parallel 7.5 mm-long straight phase modulation sections interconnected by two optical crossings and two microwave U-turns. Two optical arms of each MZM experience U-turn bends and cross mutually with low loss (measured 0.13 dB/crossing) and low crosstalk, resulting in the accumulation of phase differences at every modulation section. Thus, the actual modulation length of each MZM reaches 22.5 mm.

The folded TWEs with air bridges are the most critical part of the present device and are key to achieving a large bandwidth

and low RF reflections. The bending of the folded TWE leads to the degradation of the high-frequency response of the device owing to the introduced discontinuities and imbalances that excite the unwanted coupled slot-line mode in coplanar waveguide (CPW) circuits.²⁰ As illustrated in Fig. 1(b), at each TWE U-turn bend, the coplanar waveguide (CPW) experiences discontinuities, and the imbalances occur when the RF signal on the inner path has a shorter transmission distance than that on the outer path. These discontinuities and imbalances distort the RF wavefront and deteriorate the modulation bandwidth and RF return loss due to the excitation of the coupled slot-line mode. We address this wavefront distortion issue by implementing air bridge structures and chamfered signal electrodes, as shown in Fig. 1(c). Air bridges are widely used in monolithic microwave integrated circuits to suppress the coupled slot-line mode at TWE bends by achieving ground equalization; however, they also introduce excess shunt capacitance to the ground with the signal conductor.^{18–20} In addition, as depicted in Fig. 1(c), we employ chamfered signal electrodes to reduce the length difference between the two slots in the bent transmission lines, which will further suppress the excitation of the slot-line mode.^{21,22} Meanwhile, the chamfered bend acts as a short high-impedance transmission line that can compensate for the excess capacitance from air bridges.¹⁸

To clarify the effect of chamfered signal electrodes and air bridges, we simulate three structures, as shown in Fig. 2. First, we simulate the folded CL-TWE with the chamfered signal electrodes but without air bridges (green line). We can see that the CL-TWE suffers from significant RF loss and high reflection owing to the unequaled ground potential in the ground-signal-ground configuration, indicating the significant excitation of the radiative slot-line mode. Second, we simulate the folded CL-TWE with air bridges but without the chamfered signal electrodes (purple line). We set up two air bridges at every 90° bends. The dimension of air-bridge structures was designed as w_a of 10 μm , h_a of 0.3 μm , and h_g of 3 μm for decent shunt capacitances. Compared with the first one, the second simulation demonstrates a much lower RF loss owing to the suppression of the slot-line mode to a certain extent, although the S_{21} response curve shows fluctuations. Finally, we simulate the folded CL-TWE with air bridges together with the chamfered signal electrodes (red line). The results show that by combining the air bridges and the chamfered signal electrodes, the device exhibits a broadband and flat S_{21} curve; moreover, the RF reflection is much

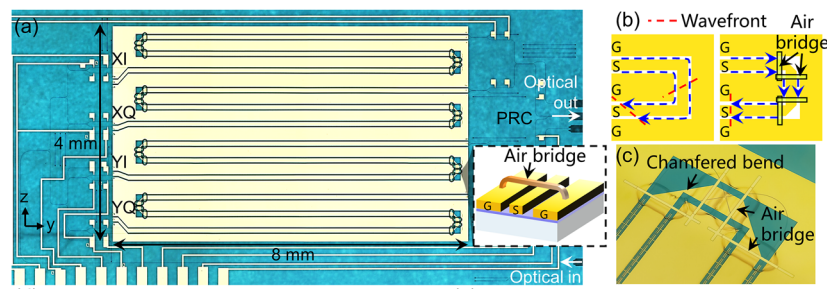


FIG. 1. (a) Microscope image of the folded DP-IQ. Inset: 3D schematic of the air bridge. (b) Schematic of the TWE U-turn bends. (c) False-color SEM image of the air-bridge-assisted U-turn TWE.

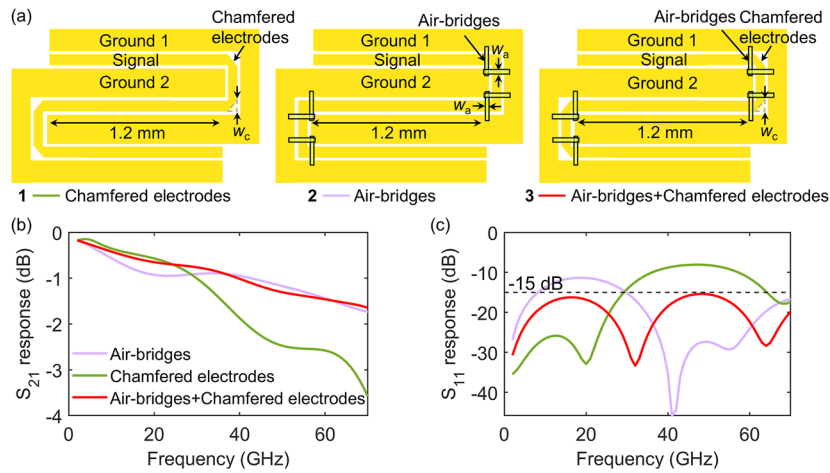


FIG. 2. (a) Schematic of the three simulated folded CL-TWEs. Simulated (b) S_{21} and (c) S_{11} parameters of the folded CL-TWEs with air-bridge structures and/or chamfered bends, respectively.

lower (<15 dB). These results show that the air bridges and chamfered electrodes improve impedance matching and reduce RF loss, indicating the effective suppression of the unwanted slot-line mode. Thus, we employ air bridges and chamfered signal electrodes at the TWE U-turns for mutual reinforcement and best high-frequency performance.

The device was fabricated on a TFLN-on-quartz platform with a 360 nm-thick LN membrane. First, we patterned and defined all optical components (such as waveguides, PRC, and MMI coupler) through e-beam lithography and inductively coupled plasma (ICP) etching processes. Then, we deposited 0.7 μm -thick SiO_2 as a buffer layer, followed by e-beam evaporation of 0.9 μm -thick gold and a lift-off process to define the CL-TWE. After that, we fabricated four gold air bridges (thickness $h_a = 300 \text{ nm}$) connecting the ground pads at each TWE U-turn. To process the air bridges, we defined the areas for air-bridge contacts on a 3 μm -thick SU-8 photoresist, followed by the evaporation of gold, defining the strip pattern and a lift-off process. Finally, we flip-chip bonded a 50 Ω terminator at the end of each CL-TWE for impedance matching.

III. DEVICE CHARACTERIZATION

A. Small-signal measurements

To indicate the effect of air bridge structures, we measured the electrical-electrical (EE) response of two folded TWEs with and without air bridge structures, respectively. Here, we use a vector network analyzer (VNA, Agilent N5227A) and standard Short-Open-Load-Through (SOLT) calibration method to characterize the EE response up to 67 GHz. As shown in Fig. 3(a), the air-bridge-assisted TWE exhibits a much flatter electrical-electrical (EE) S_{21} response and much lower S_{11} return loss. Obviously, the air bridges suppress the excitation of the lossless slot-line mode that will bring extra loss in transmission and high reflection.

We also measured the EO response of the four MZMs in the presented DP-IQ. The input light from a tunable laser of wavelength 1550 nm through a polarization controller (PC) was coupled into the

DP-IQ chip through an edge coupler [input port in Fig. 1(a)]. The small RF signal from the VNA was sent to the chip through a probe. Then, we collected the modulated light through the grating coupler at the output of each sub-MZM and sent it to the 70 GHz high-speed photodetector and received it by the VNA. As shown in Fig. 3(b), the 3 dB EO modulation bandwidths are all larger than 67 GHz. The four MZMs have a uniform and relatively flat EO response that

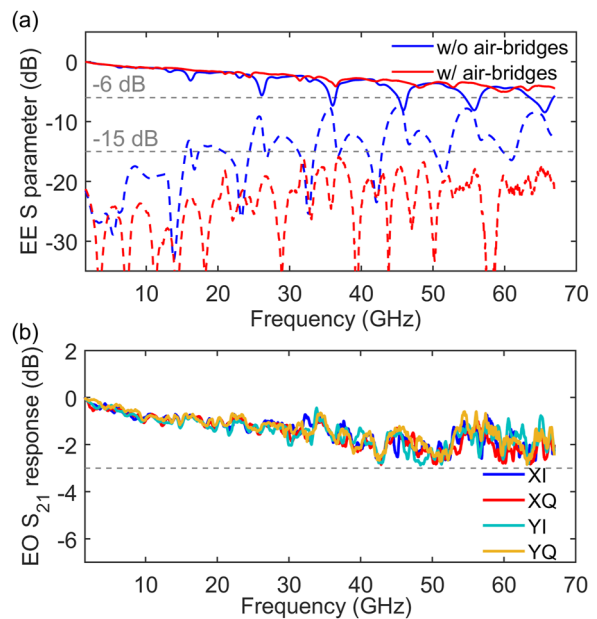


FIG. 3. (a) Measured EE S_{21} (solid lines) and S_{11} (dashed lines) of the TWEs with (w/) and without (w/o) air-bridges. (b) Measured EO S_{21} response of the four MZMs.

will relax the digital signal processing (DSP) cost and provide better performance in long-haul transmissions.

B. Long-haul transmission

The present DP-IQ modulator is evaluated in a long-haul transmission link as the channel under test (CUT) at a frequency of 194.2 THz and is multiplexed with ten other channels using a commercial coherent driver modulator (CDM) [Fig. 4(a)]. Each channel comprises eight digital Nyquist subcarriers (SCs) and supports a 95 Gbaud probabilistic constellation-shaped (PCS) 16QAM data stream, which provides a line data rate of 703 Gb/s at an average information rate of 7.4 bits/symbol for dual polarization. The Nyquist subcarrier was adopted here to increase the tolerance to

chromatic dispersion and nonlinear impairments, thereby further increasing the capacity–reach product.^{23,24} At the transmitter DSP, 8×11.875 GBaud 16QAM symbols with probability constellation shaping are distributed equally in the frequency domain. Subsequently, the transmitter impairments, which include amplitude imbalance, phase imbalance, in-phase, and quadrature skew are fully compensated across the entire bandwidth. At the receiver DSP, each subcarrier undergoes the same signal processing: digitally down-converted to the baseband, 2×2 MIMO adaptive equalization, and carrier recovery. Note that our device was directly driven by a 120 Gsa/s arbitrary waveform generator (AWG) with an actual peak-to-peak voltage (V_{pp}) of 516 mV without using any RF amplifiers. The transmission link consisted of 14×80 km standard single-fiber spans (G.652.D), and each began with a variable optical attenuator

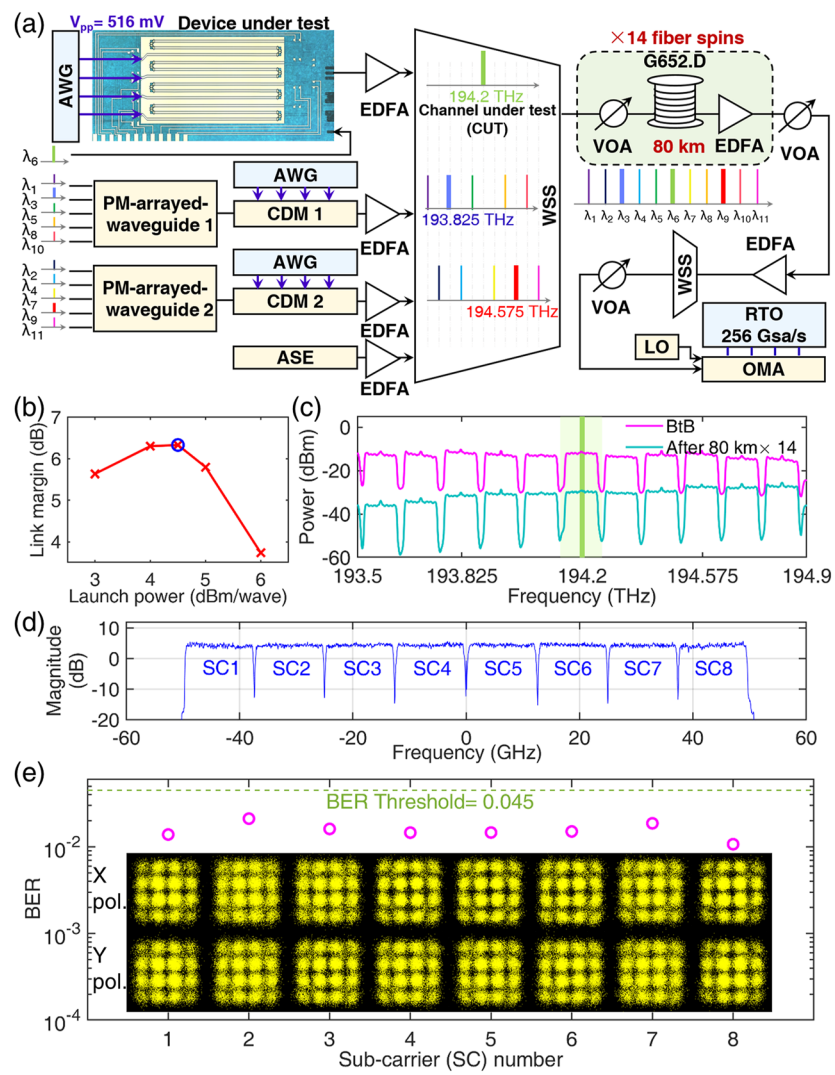


FIG. 4. (a) Experimental setup. (b) Link margin as a function of the launch power. (c) Optical spectra of all 11 channels before and after the fiber links. (d) and (e) Received spectrum of the CUT and corresponding constellations and BERs after 1120 km transmission, respectively.

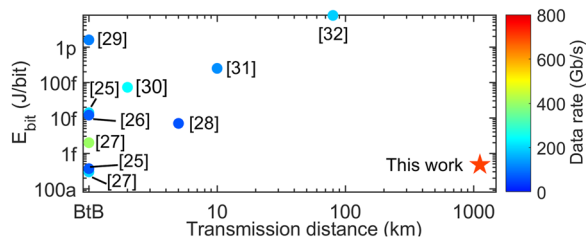


FIG. 5. Recent ultralow-energy data transmission exceeding 56 Gb/s.^{25–31}

(VOA) and followed by an erbium-doped fiber amplifier (EDFA) to set the launch power in the fiber link. Figure 4(a) shows the measured link margin as a function of launch power for all channels after transmission over the 1120 km fiber link. We realize the optimal transmission performance with the largest link margin of 6.33 dB at a launch power of 4.5 dBm [blue circle in Fig. 4(b)].

Figure 4(c) shows the corresponding transmitted spectra before and after the fiber transmission. Figure 4(d) shows the received spectrum of the CUT with good power uniformity, thanks to the high EO bandwidth of the present device. The corresponding constellations and bit-error rates (BERs) of all eight digital SCs after 1120 km transmission are shown in Fig. 4(e). The BERs of all SCs were below the 25% forward error correction (FEC) threshold, resulting in a net data rate of 562 Gb/s.

Benefiting from the low driving voltage and operation without RF amplifiers, the present device exhibits a record-low electrical energy consumption: $E_{\text{bit}} = 4V_{\text{rms}}^2 / (\text{Bit-rate} \times R) = 4 \times (0.0649)^2 / (703 \times 10^9 \times 50) = 479 \text{ aJ/bit}$. To the best of our knowledge, this is the lowest value for long-haul transmissions ever reported thus far for EO modulators (Fig. 5).^{25–31}

IV. CONCLUSION

In conclusion, we propose a folded architecture for a TFLN-based DP-IQ modulator, featuring a CMOS-compatible drive voltage, large modulation bandwidth, and compact device footprint. Among CMOS-level-voltage folded modulators (Table I), our device achieves the highest bandwidth and transmission rate.^{13–17} To our knowledge, our compact device allows for attojoule-per-bit level electrical energy consumption, for the first time, in transmissions over distances above 1000 km, paving the way for capacity-intensive and cost-effective optical networks.

We noted that the total size of the modulator is not decreased with the folded architecture. However, our shorter device provides a promising solution for fitting into modern transceiver modules such as Small Form-factor Pluggable and Quad Small Form-factor Pluggable, as well as photonics integrated circuits (PICs). The processing procedure for the air bridges and proposed folded modulators is well-suited to photolithography techniques, enabling future scalable production. Future work will be dedicated to integrating the multi-functional TFLN-based device (optical frequency combs,^{33,34} nonlinear devices,³⁵ etc.) and III-V-on-TFLN active device (lasers,³⁶ photodetectors,³⁷ etc.) toward achieving high-performance PICs.

ACKNOWLEDGMENTS

This work was supported by the National Key Research and Development Program of China (Grant No. 2019YFA0705004), Innovation Program for Quantum Science and Technology (Grant No. 2021ZD0301500), and Natural Science Foundation of China (Grant No. 62293523).

AUTHOR DECLARATIONS

Conflict of Interest

The authors have no conflicts to disclose.

Author Contributions

Mengyue Xu and Yuntao Zhu contributed equally to this work.

Mengyue Xu: Conceptualization (lead); Data curation (lead); Formal analysis (lead); Investigation (lead); Methodology (lead); Project administration (equal); Validation (lead); Writing – original draft (lead); Writing – review & editing (equal). **Yuntao Zhu:** Data curation (supporting); Formal analysis (supporting); Investigation (equal). **Jin Tang:** Data curation (supporting); Formal analysis (supporting); Investigation (supporting); Resources (supporting); Software (supporting); Writing – original draft (supporting). **Jingyi Wang:** Investigation (supporting). **Lin Liu:** Investigation (supporting). **Huixiao Ma:** Resources (supporting). **Siyuan Yu:** Funding acquisition (supporting); Writing – review & editing (supporting). **Bofang Zheng:** Investigation (supporting); Resources (supporting);

TABLE I. Comparison of folded TFLN modulators.

	$BW_{3\text{dB}}$ (GHz)	V_{π} (V)	Physical length (mm)	Data rate (Gb/s) [E_{bit} (fJ/bit)]
13	45	0.7	11	200/4.49
14	43	1.08	8	N.A.
15	37.5	4	5	N.A.
16	40	1.24	8.7	128/N.A.
17	55	3.6	>5	N.A.
This work	>67	1	8	703/0.479

Writing – review & editing (supporting). **Xinlun Cai:** Conceptualization (equal); Funding acquisition (lead); Project administration (lead); Resources (lead); Supervision (lead); Writing – review & editing (lead).

DATA AVAILABILITY

The data that support the findings of this study are available from the corresponding author upon reasonable request.

REFERENCES

- ¹Infinera, Baud Rate, Modulation, and Maximizing Coherent Optical Performance, 2021.
- ²K. Kikuchi, “Fundamentals of coherent optical fiber communications,” *J. Lightwave Technol.* **34**, 157–179 (2016).
- ³A. Moscoso-Martir, J. Koch, O. Schulz, J. Muller, A. T. Mashayekh, A. D. Das, F. Merget, S. Pachnicke, and J. Witzens, “Silicon photonic integrated circuits for soliton based long haul optical communication,” *J. Lightwave Technol.* **40**, 3210–3222 (2022).
- ⁴M. Luo, C. Yang, H. Zhang, L. Wang, Z. He, X. Xiao, and S. Yu, “Experimental demonstration of long-haul transmission using silicon-based IC-TROSA,” *IEEE Photonics Technol. Lett.* **34**, 862–865 (2022).
- ⁵Y.-W. Chen, S. Yi, G. Ling, B. West, L. Zhao, and W. I. Way, “Real-time demonstration of 75 GHz-spaced DWDM single-carrier 400G CFP2-DCO over 1500 km,” *J. Lightwave Technol.* **40**, 1375–1381 (2022).
- ⁶S. Porto, M. Chitgarha, I. Leung, R. Maher, R. Going, S. Wolf, P. Studenkov, J. Zhang, H. Hodaei, T. Frost, H.-S. Tsai, S. Buggaveeti, A. Rashidinejad, A. Yekani, R. Mirzaei Nejad, M. Iglesias Olmedo, S. Kerns, J. Diniz, D. Pavinski, R. Brigham, B. Foo, M. Al-Khateeb, S. Koenig, P. Samra, M. Missey, V. Dominic, H. Sun, S. Sanders, J. Osenbach, S. Corzine, P. Evans, V. Lal, and M. Ziari, “Demonstration of a 2×800 Gb/s wave coherent optical engine based on an InP monolithic PIC,” *J. Lightwave Technol.* **40**, 664–671 (2022).
- ⁷F. Pittalà, R.-P. Braun, G. Boeckerer, P. Schulte, M. Schaeddler, S. Bettelli, S. Calabro, M. Kuschnerov, A. Gladisch, F.-J. Westphal, C. Xie, R. Chen, Q. Wang, and B. Zheng, “Single-carrier coherent 930G, 1.28T and 1.60T field trial,” in *2021 European Conference on Optical Communication (ECOC)* (IEEE, 2021).
- ⁸M. Nakamura, T. Sasai, T. Kakizaki, F. Hamaoka, T. Kobayashi, E. Yamazaki, and Y. Kisaka, “Impact of local oscillator phase noise on long-haul transmission of 120-Gbaud digital sub-carrier signals,” in *Optical Fiber Communications Conference and Exhibition (OFC)* (Optica Publishing Group, 2022).
- ⁹M. Xu, Y. Zhu, F. Pittalà, J. Tang, M. He, W. C. Ng, J. Wang, Z. Ruan, X. Tang, M. Kuschnerov, L. Liu, S. Yu, B. Zheng, and X. Cai, “Dual-polarization thin-film lithium niobate in-phase quadrature modulators for terabit-per-second transmission,” *Optica* **9**, 61–62 (2022).
- ¹⁰Y. Xue, R. Gan, K. Chen, G. Chen, Z. Ruan, J. Zhang, J. Liu, D. Dai, C. Guo, and L. Liu, “Breaking the bandwidth limit of a high-quality-factor ring modulator based on thin-film lithium niobate,” *Optica* **9**, 1131–1137 (2022).
- ¹¹P. Kharel, C. Reimer, K. Luke, L. He, and M. Zhang, “Breaking voltage-bandwidth limits in integrated lithium niobate modulators using micro-structured electrodes,” *Optica* **8**, 357–363 (2021).
- ¹²M. Xu, M. He, H. Zhang, J. Jian, Y. Pan, X. Liu, L. Chen, X. Meng, H. Chen, Z. Li, X. Xiao, S. Yu, S. Yu, and X. Cai, “High-performance coherent optical modulators based on thin-film lithium niobate platform,” *Nat. Commun.* **11**, 3911 (2020).
- ¹³G. Chen, K. Chen, J. Zhang, R. Gan, L. Qi, X. Fan, Z. Ruan, Z. Lin, J. Liu, C. Lu, A. P. Tao Lau, D. Dai, C. Guo, and L. Liu, “Compact 100 GBaud driverless thin-film lithium niobate modulator on a silicon substrate,” *Opt. Express* **30**, 25308–25317 (2022).
- ¹⁴X. Liu, H. Liu, B. Xiong, C. Sun, Z. Hao, L. Wang, J. Wang, Y. Han, H. Li, and Y. Luo, “Broadband meandered thin-film lithium niobate modulator with ultra-low half-wave voltage,” *IEEE Photonics Technol. Lett.* **34**, 424–427 (2022).
- ¹⁵S. Nelan, A. Mercante, C. Hurley, S. Shi, P. Yao, B. Shopp, and D. W. Prather, “Compact thin film lithium niobate folded intensity modulator using a waveguide crossing,” *Opt. Express* **30**, 9193–9207 (2022).
- ¹⁶S. Sun, M. Xu, M. He, S. Gao, X. Zhang, L. Zhou, L. Liu, S. Yu, and X. Cai, “Folded heterogeneous silicon and lithium niobate Mach-Zehnder modulators with low drive voltage,” *Micromachines* **12**, 823 (2021).
- ¹⁷J. Hu, C. Li, C. Guo, C. Lu, A. P. T. Lau, P. Chen, and L. Liu, “Folded thin-film lithium niobate modulator based on a poled Mach-Zehnder interferometer structure,” *Opt. Lett.* **46**, 2940–2943 (2021).
- ¹⁸T. M. Weller, R. M. Henderson, K. J. Herrick, S. V. Robertson, R. T. Kihm, and L. P. B. Katehi, “Three-dimensional high-frequency distribution networks. I. Optimization of CPW discontinuities,” *IEEE Trans. Microwave Theory Tech.* **48**, 1635–1642 (2000).
- ¹⁹J. R. Miller, J. E. Harriss, and L. W. Pearson, “Micromachining of air-bridges on SU-8 substrates,” *IEEE Trans. Compon. Packag. Technol.* **31**, 159–164 (2008).
- ²⁰G. E. Ponchak, J. Papapolymerou, and M. M. Tentzeris, “Excitation of coupled slotline mode in finite-ground CPW with unequal ground-plane widths,” *IEEE Trans. Microwave Theory Tech.* **53**, 713–717 (2005).
- ²¹P. M. Watson and K. C. Gupta, “Design and optimization of CPW circuits using EM-ANN models for CPW components,” *IEEE Trans. Microwave Theory Tech.* **45**, 2515–2523 (1997).
- ²²Y. Tian, N. Li, H. Wang, X. P. Li, and K. Y. Lee, “Right-angled microcoaxial bends for Si-based RF/microwave integrated circuits,” *IEEE Trans. Compon. Packag. Technol.* **6**, 290–297 (2016).
- ²³H. Sun, M. Torbatian, M. Karimi, R. Maher, S. Thomson, M. Tehrani, Y. Gao, A. Kumpara, G. Soliman, A. Kakkar, M. Osman, Z. A. El-Sahn, C. Doggart, W. Hou, S. Sutarwala, Y. Wu, M. R. Chitgarha, V. Lal, H.-S. Tsai, S. Corzine, J. Zhang, J. Osenbach, S. Buggaveeti, Z. Morbi, M. I. Olmedo, I. Leung, X. Xu, P. Samra, V. Dominic, S. Sanders, M. Ziari, A. Napoli, B. Spinnler, K.-T. Wu, and P. Kandappan, “800G DSP ASIC design using probabilistic shaping and digital sub-carrier multiplexing,” *J. Lightwave Technol.* **38**, 4744–4756 (2020).
- ²⁴M. Torbatian, D. Lavery, M. Osman, D. Yao, D. S. Millar, Y. Gao, A. Kakkar, Z. A. El-Sahn, C. Doggart, A. E. Morra, N. Abughaleh, S. Yang, X. Chen, R. Maher, H. Sun, K.-T. Wu, and P. Kandappan, “Performance oriented DSP for flexible long haul coherent transmission,” *J. Lightwave Technol.* **40**, 1256–1272 (2022).
- ²⁵C. Wang, M. Zhang, X. Chen, M. Bertrand, A. Shams-Ansari, S. Chandrasekhar, P. Winzer, and M. Lončar, “Integrated lithium niobate electro-optic modulators operating at CMOS-compatible voltages,” *Nature* **562**, 101–104 (2018).
- ²⁶C. Haffner, D. Chelladurai, Y. Fedoryshyn, A. Josten, B. Baeuerle, W. Heni, T. Watanabe, T. Cui, B. Cheng, S. Saha, D. L. Elder, L. R. Dalton, A. Boltsasseva, V. M. Shalaev, N. Kinsey, and J. Leuthold, “Low-loss plasmon-assisted electro-optic modulator,” *Nature* **556**, 483–486 (2018).
- ²⁷W. Heni, Y. Fedoryshyn, B. Baeuerle, A. Josten, C. B. Hoessbacher, A. Messner, C. Haffner, T. Watanabe, Y. Salamin, U. Koch, D. L. Elder, L. R. Dalton, and J. Leuthold, “Plasmonic IQ modulators with attojoule per bit electrical energy consumption,” *Nat. Commun.* **10**, 1694 (2019).
- ²⁸R. Dubé-Demers, S. LaRochelle, and W. Shi, “Ultrafast pulse-amplitude modulation with a femtojoule silicon photonic modulator,” *Optica* **3**, 622–627 (2016).
- ²⁹K. Li, S. Liu, D. J. Thomson, W. Zhang, X. Yan, F. Meng, C. G. Littlejohns, H. Du, M. Banakar, M. Ebert, W. Cao, D. Tran, B. Chen, A. Shakoor, P. Petropoulos, and G. T. Reed, “Electronic-photonic convergence for silicon photonics transmitters beyond 100 Gbps on-off keying,” *Optica* **7**, 1514–1516 (2020).
- ³⁰M. Jacques, Z. Xing, A. Samani, E. El-Fiky, X. Li, M. Xiang, S. Lessard, and D. V. Plant, “240 Gbit/s silicon photonic Mach-Zehnder modulator enabled by two 2.3-Vpp drivers,” *J. Lightwave Technol.* **38**, 2877–2885 (2020).
- ³¹A. Samani, E. El-Fiky, M. Morsy-Osman, R. Li, D. Patel, T. Hoang, M. Jacques, M. Chagnon, N. Abadia, and D. V. Plant, “Silicon photonic Mach-Zehnder modulator architectures for on chip PAM-4 signal generation,” *J. Lightwave Technol.* **37**, 2989–2999 (2019).
- ³²I. G. López, A. Aimone, S. Alreesh, P. Rito, T. Brast, V. Höhns, G. Fiol, M. Gruner, J. K. Fischer, J. Honecker, A. G. Steffan, D. Kissinger, A. C. Ulusoy, and M. Schell, “DAC-free ultralow-power dual-polarization 64-QAM transmission at 32 GBd with hybrid InP IQ SEMZM and BiCMOS drivers module,” *J. Lightwave Technol.* **35**, 404–410 (2017).
- ³³Y. Hu, M. Yu, B. Buscaino, N. Sinclair, D. Zhu, R. Cheng, A. Shams-Ansari, L. Shao, M. Zhang, J. M. Kahn, and M. Lončar, “High-efficiency and broadband on-chip electro-optic frequency comb generators,” *Nat. Photonics* **16**, 679–685 (2022).

³⁴M. Xu, M. He, Y. Zhu, S. Yu, and X. Cai, “Flat optical frequency comb generator based on integrated lithium niobate modulators,” *J. Lightwave Technol.* **40**, 339–345 (2022).

³⁵M. G. Vazimali and S. Fathpour, “Applications of thin-film lithium niobate in nonlinear integrated photonics,” *Adv. Photonics* **4**, 034001 (2022).

³⁶Y. Han, X. Zhang, R. Ma, M. Xu, H. Tan, J. Liu, R. Wang, S. Yu, and X. Cai, “Widely tunable O-band lithium niobite/III–V transmitter,” *Opt. Express* **30**, 35478–35485 (2022).

³⁷X. Zhang, X. Liu, R. Ma, Z. Chen, Z. Yang, Y. Han, B. Wang, S. Yu, R. Wang, and X. Cai, “Heterogeneously integrated III–V-on-lithium niobate broadband light sources and photodetectors,” *Opt. Lett.* **47**, 4564–4567 (2022).